Overheating, flame, smoke, and freight movement detection algorithms based on charge-coupled device camera for aircraft cargo hold surveillance

Thierry Sentenac, Yannick Le Maoult, Jean-José Orteu, G Boucourt

Overheating, flame, smoke, and freight movement detection algorithms based on charge-coupled device camera for aircraft cargo hold surveillance

Thierry Sentenac
Yannick Le Maoult
Jean-José Orteu
Ecole des Mines d'Albi-Carmaux
Route de Teillet
81013 Albi CT Cedex 09, France
E-mail: sentenac@enstimac.fr

Gérard Boucourt
Latécoère
35 rue de Périole, BP 5211
31079 Toulouse Cedex 5, France

Abstract. We introduce a new approach to aircraft cargo compartment surveillance. The originality of the approach is in the use of a single sensor type, a CCD camera, to detect fire events and freight movement in aircraft cargo holds (multiphenomenom/monosensor approach). The CCD camera evaluation and the radiometric and geometric models are provided in (Sentenac et al., 2002). We go on to discuss the image analysis algorithms used in the detection of fire signatures (hot spots, flame, and smoke) and load displacement. For each phenomenon, the discriminant parameters are established and the algorithm is explained. The crucial factor is the validation procedure according to aeronautical standards. The experimental trials were carried out in a test chamber providing the fire and smoke test facilities [TF1 to TF6 following EN 54 (Afnor, 1997) requirements].

Subject terms: detection; sensors; surveillance; image analysis; charge-coupled devices.

1 Introduction

The work presented in this paper forms part of a load video surveillance system project carried out in parallel with European projects.[1,2] The overall objective is to develop a new, more effective surveillance approach to the detection of fire events and freight movement in aircraft cargo holds.

Fire events are defined as the different signatures of the combustion process that releases energy and produces gaseous, solid, and condensed liquid emissions. The energy released and the products formed depend on the composition of combusting materials, the oxygen concentration, the mode of combustion, and so on. In any case, the pyrolysis reaction is the first step of the combustion process. This step involves the heating of the material surface and the production of smoke and gases. This can lead to the next step in the pyrolysis reaction: the evolution into flaming fire. Whereas certain solids will often remain in the smoldering mode of combustion, certain liquid materials can evolve rapidly and dramatically into flame. The materials involved in cargo compartment fires are as varied as the cargo being transported: cardboard boxes, clothes, soft nylon or rigid plastic suitcases, fuel, etc. To conclude, the candidate fire signatures for early fire detection are instance of overheating (see Fig. 1), smoke (see Fig. 2), and flame (see Fig. 3).

In certain special air-freight sectors, such as transport of aircraft sections, satellites, etc. (see Fig. 4, the Airbus A300-600ST Super Transporter, known as "The Beluga") surveillance of freight displacement can be the more crucial concern. Freight movements can arise due to faulty stowage procedures in the cargo area.

Fire events or freight movements represent two of the most dangerous situations in an aircraft hold, and their early detection by surveillance systems is crucial. At the activation of the fire alarm the pilot must immediately activate the halon fire extinguishing system and will be potentially obliged to make an emergency landing. However, according to the Federal Aviation Administration,[3] on board commercial aircraft, the ratio of false to genuine alarms is estimated as high as 500:1. This situation is highly undesirable as it leads to the emptying of the halon stock, which may be needed for a subsequent real fire, and the risks involved in emergency landings are considerable due to a wide variety of factors: the pilot's unfamiliarity with the airport, inferior navigation aids, shorter runways, etc. Up to now, the surveillance systems most commonly used in cargo areas are based on the smoke detectors, which sense the presence of aerosols (radioactive ionization and photoelectric light attenuation detectors). This means the presence of fire is detected by one fire signature only. By adding thermal sensors, the detection of the heat fire signature improves awareness, but the time response limits performance. It seems clear that a multisensor/multicriteria approach, enabling detection of all fire signatures is the way ahead. Another problem is that the pilot is not able to verify the occurrence or the state of a real fire in an unaccessible cargo compartment during flight. Very early on, some researchers suggested monitoring the cargo hold with imaging systems combined with conventional detection

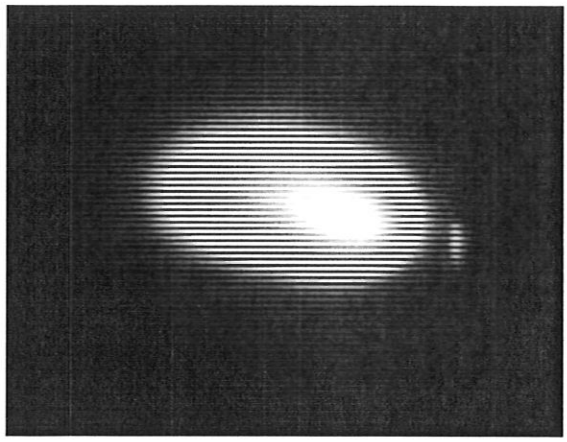

Fig. 1 Image of a simulated smoldering fire in near infrared spectral band.

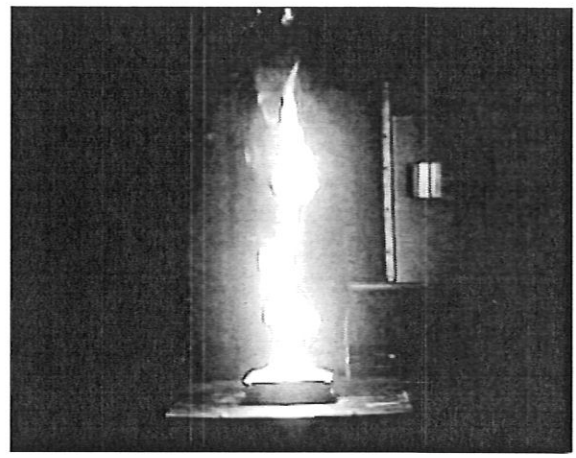

Fig. 3 Image of a gasoline flame in visible spectral band.

systems.[4,5] Afterward, overheating, flame presence, and smoke concentration measurement capabilities were added to various imaging systems[6–8] (color video, IR, and microbolometer cameras). The result is a multipurpose machine vision based on different imaging system technologies, capable of detecting smoldering, flame, and smoke situations.[9]

A fire detection system based on imaging systems can cover wide areas of observation and allows visual inspection by the pilot. However, while increasing the number of detection parameters by adding different imaging technologies improves detection efficiency, it also increases costs and limits the maintenance capability of the system. Rather than relying on combinations of sensors, the proposed new fire-surveillance system is based on one single CCD technology capable of monitoring the whole area and of detecting all possible fire signatures. To ensure this, the new system is supplemented by detect and track movement capabilities covering the entire cargo area.

The proposed new video surveillance system is based on a single CCD technology with multi-measurement capabilities. Reference 10 characterizes the CCD sensor, referred to as the video sensor unit[11] (VSU) (see Fig. 5), which operates in the near-IR spectral. The paper is organized as follows. Section 2 describes the overheat detection algorithm and its validation in different situations. Next, Sec. 3 gives the principle of the smoke detection algorithm. Section 4 presents and justifies the parameters chosen in the flame detection algorithm. The results of the tests conducted using liquid and solid fuels in flaming combustion (kerosene, wood, paper, etc.) are discussed. These algorithms are used in parallel together to significantly enhance the accuracy of the fire detection. For example, the system can enter alert mode after an overheating detection or after a smoke-only detection in cases of hidden fires. Finally, Sec. 5 provides the movement detection algorithm and explains the computation of the displacement between two successive 3-D localizations of the freight in the cargo hold.

2 Overheat Detection Algorithm

The initial phase of the combustion process is the pyrolysis reaction, which represents the smoldering mode of combus-

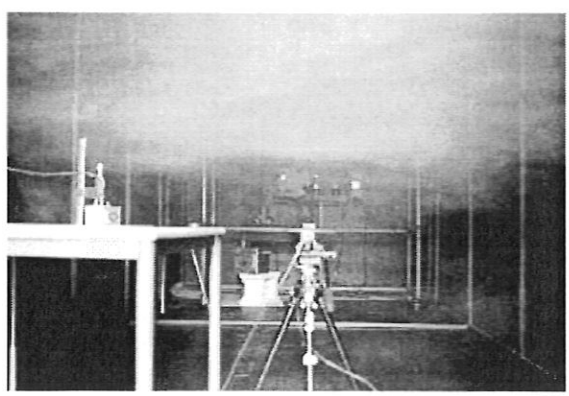

Fig. 2 Image of smoke phenomenon in visible spectral band.

Fig. 4 Satellite transportation (airbus).

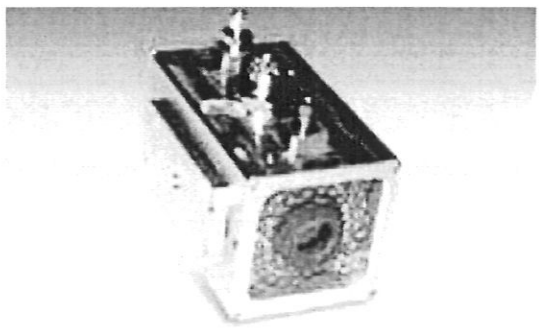

Fig. 5 Video sensor unit (Latécoère).

tion. It is characterized[12] by a heat increase with a temperature of 200 to 600°C. The duration of the hot spots can vary from a few seconds to several minutes. This duration depends on the flight conditions (concentration of oxygen, pressure, etc.) and the type of fuel.

The performance objective of the video camera is to sense rapidly a temperature increasing from 200°C with a tolerance of ±12.5%. Note that a temperature in excess of 600°C would be considered as a flame temperature. The lower limit of the detected hot spot size is 50 mm at an observation distance of 15 m. After the detection of the hot spot, the image processing software must identify and track the overheat condition by estimating the temporal and spatial gradients of the hot spot's temperature.

In aircraft applications, the overheat situations can generally be detected by sensing the change in the thermal environment with temperature sensitive resistance. Temperature measurement, combined with smoke sensors, improves the detection of nearly smoke-less fires.[13] The approach is available from a large number of manufacturers. In contrast, the direct heat flux produced by hot spots is rarely measured in aircraft applications. Thus, photodetectors can quickly respond to the incident flux from the hot source. The remaining problem is to evaluate sensor sensitivity at low temperatures, and this becomes more complex with a CCD detector.[10]

First, this section begins with principal results on the configuration and the calibration proposed for the CCD detector. The section then describes the algorithm principle for detecting and measuring the temporal gradient of temperature over detected hot spots. Next, the section analyzes the influence of the hot source type, the measurement situation, and the environment transmittance by computing the resulting temperature uncertainty. Finally, the algorithm performances are discussed.

2.1 *Configuration and Calibration of the Camera*

The ability of a camera system to detect a low temperature depends mainly on the sensitivity of the camera sensor to radiation generated by hot spot relative to camera noise sources. For low-cost CCD imaging systems operating in near-IR (NIR) spectral band (0.75 to 1.1 μm), Ref. 10 determines that a minimal temperature of 330°C can be detected with a low optical system f-number of 1.4 and an integration time t_i of 360 ms. The integration time respects a total detection time of 3 s in accordance with our surveillance application requirements. Note that the temperature value is higher than the minimal smoldering fire temperature and limits the overheat detection algorithm capability. Then, as the hot sources temperature increases the sensor signal increases with a possible saturation. The ability of sensors to measure the temperature ranging from 330 to 600°C is obtained by varying the exposure time ranging from 360 to 1 ms (see Figs. 6 and 7).

Reference 10 provides also the CCD camera radiometric model and the calibration procedure. In the temperature range under concern (330 to 600°C), the principal result is a temperature sensitivity that rises rapidly from 0.3 to 7.25 gray levels/°C and a maximal noise equivalent temperature difference (NETD), which is measured as being ±4°C.

2.2 *Detection Principle*

In the high sensitivity of the sensor (t_i=360 ms), the overheat situations are detected in the image when the digital output camera I_D is greater than three times the standard deviation σ_{I_D} of the noise signal. For our system with a digitizer of 8 bits, the noise fluctuations represent a standard deviation σ_{I_D} of 1 gray level. This threshold corresponds to the minimal temperature of 330°C. Note that the standard deviation of the noise signal is also estimated for each exposure time.

After detection, the image pixels corresponding to this minimal temperature are labeled overheat region of interest (OROI) for hot spots (see Figs. 8 and 9). The minimal and maximal digital intensity, number, size, and barycenter of

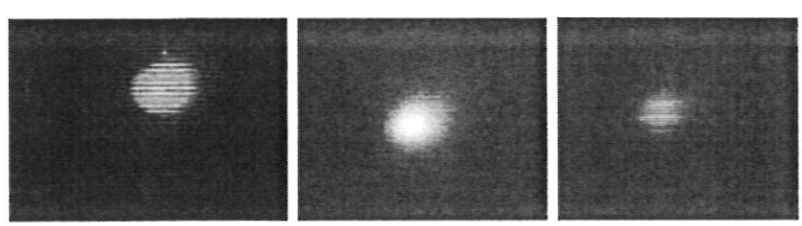

$ti = 360ms$ $ti = 20ms$ $ti = 1ms$

Fig. 6 Evolution of an overheat situation with a surface of diameter 65 mm at an observation distance of 3 m with different exposure times in the NIR spectral band.

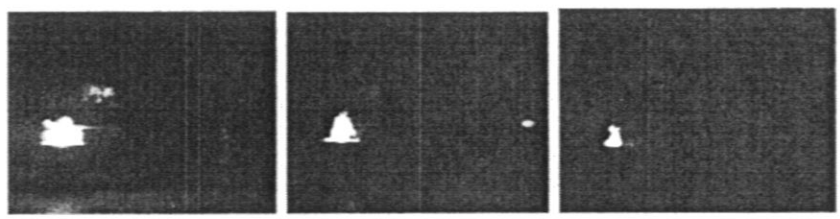

$ti = 360ms$ $ti = 20ms$ $ti = 1ms$

Fig. 7 Beginning of a kerosene fire with a based surface of diameter 120 mm at an observation distance of 3 m and different exposure times in NIR spectral band.

each overheat event are computed from each image acquired (for each exposure time $t_i = 360$, 20, and 1 ms). Note that a part of the phenomenon can be saturated in the high-sensitivity image and not in the low-sensitivity image. Regions with a surface lower than 3 pixels are eliminated (from the projection geometry considerations, the pixel surface corresponds to a surface of diameter 1 cm at an observation distance of 15 m).

For each image acquired and in each OROI, the radiometric model of the camera, previously calibrated, maps the measured intensity values I_D of only the nonsaturated pixels to equivalent blackbody temperature values T as is given by

$$T = \frac{B}{\ln[(At_i/I_D - C) + 1]}, \tag{1}$$

where A, B, and C are the parameters of the radiometric model, which was previously determined experimentally in the specific off-line calibration procedure described in Ref. 10.

The determination of the hot spot absolute temperature T_s involves correcting the equivalent blackbody temperature by the emissivity (ϵ), the location of the hot source [$\cos(\theta_d)$] and the environment transmittance (τ_e). Note that θ_d is the angle between the source-camera axis and the normal direction of the CCD detector. To this end, Eq. (1) should be modified as follows:

$$T_s = \frac{B}{\ln[(A\epsilon\tau_e \cos(\theta_d)t_i)/(I_D - C) + 1]}. \tag{2}$$

Moreover, if the source of the scene is not under focus, the source-camera distance (d_s) must be introduced in Eq. (2). Except for τ_e, which can be estimated by the measurement of the reflection coefficient of a known remote target illuminated by an emitting IR source (see the smoke detection algorithm in Sec. 3), it is difficult to control the other parameters. Therefore, an absolute uncertainty is associated with each temperature to represent the worst case (see Fig. 10). The uncertainty is computed from the radiometric model and from experiments carried out to analyze the uncertainty of each influencing parameter. If the absolute temperature is greater than 600°C and rate of increase in tem-

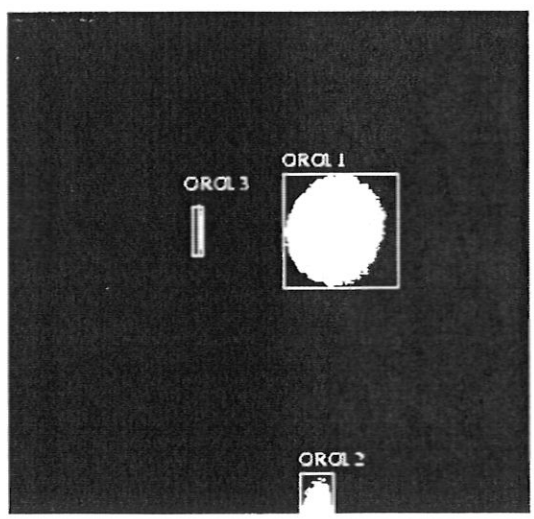

Fig. 8 Labeled image in an overheat situation.

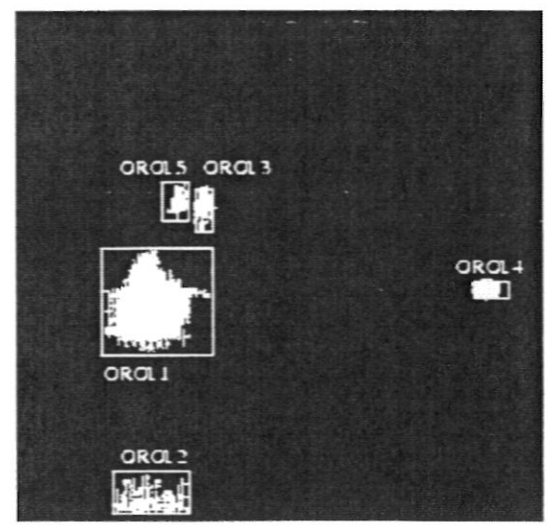

Fig. 9 Labeled image in a beginning fire.

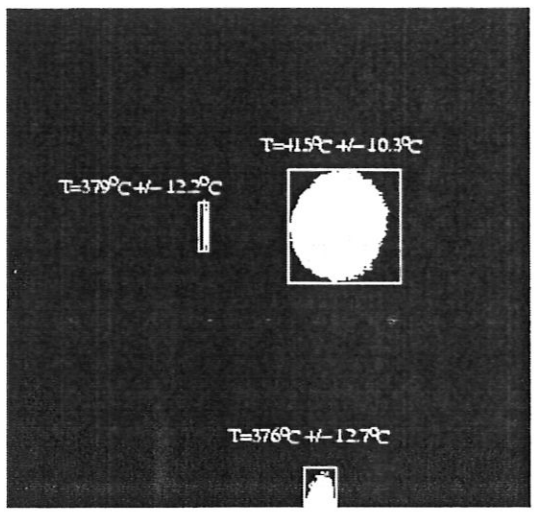

Fig. 10 Thermal image of the overheat situation.

perature and size are significant, the flame algorithm is activated to investigate a flame situation (see Sec. 4).

2.3 *Performances Evaluation*

Experiments are performed in a cargo test cell as shown in the image of Fig. 11. The position of sensors within the simulated cargo compartment is optimized to cover all accessible surfaces of containers and lining. This configuration permits monitoring and detecting hot spots between both containers and between containers and lining.

First, the heated objects in the hold are generated with blackbodies at temperature T_{ref} ranging from 300 to 600°C. The specific experiment, shown in Fig. 12, is composed of an optical test bench where the distance and the orientation between the sensor and the blackbody can be adjusted. The blackbody cavity aperture can be modified to test different overheat sizes of diameter ranging from 5 to 65 mm. At a distance of 1.5 and 6 m, the detection overheat algorithm detects a blackbody placed in front of the sensor at a temperature of 330°C. Moreover, the temperature T measured by the system is compared to reference blackbody temperature T_{ref} according to the following criterion:

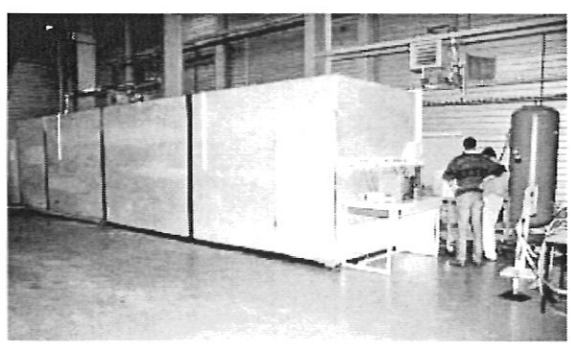

Fig. 11 Cargo test cell (12×3×3 m^3).

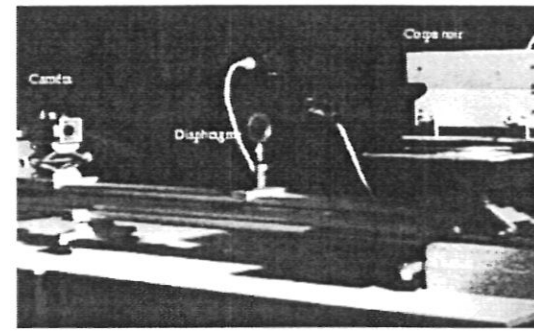

Fig. 12 Overheat test.

$$\frac{\Delta T}{T} = \frac{|T_{\text{ref}} - T|}{T_{\text{ref}}}. \tag{3}$$

2.3.1 *Temperature measurement*

The blackbody was placed at a distance of 3 m from the camera and it generated hot spots at temperature ranging from 350 to 575°C with increments of 25°C. Table 1 proves that the relative temperature error is less than 1.5%.

2.3.2 *Influence of the blackbody-camera distance*

The previous tests were repeated with the blackbody placed at different distances of the camera, respectively, 4, 6, 8, and 10 m. The temperature relative error $\Delta T/T$ was found to be less than 6.5%. Note that the blackbody surface represents an area of 37 pixels at the distance of 10 m. It was supposed that there were no effects from smoke or fog absorption.

2.3.3 *Influence of the emissivity*

Additional tests were performed to consider the influence of overheat emissivity in Eq. (2). In fact, in aircraft cargo compartments, the usual objects are often made of metal, wood, cardboard, plastic, and textiles. In the NIR spectral band, they are considered as opaque and gray bodies with a constant emissivity ranging from 0.4 to 0.97 (see Table 2). Therefore, the hot objects were simulated by a hot copper sheet (see Fig. 13) with four different emissivity areas in the range of Table 2. The real emissivity values are summarized in the Table 3. The 0.1×0.1-m^2 sheet of 0.01-m thickness was warmed up at a temperature T_{ref}, which was regulated by a thermocouple associated to a controller. The experiments were carried out with a sheet temperature of 425°C and a sensor exposure time of 360 ms. This experimental configuration provides the maximal sensor sensitivity to the measured temperatures T_i of each area.

These temperatures were compared to the reference copper temperature T_{ref}. Next, the relative temperature uncertainty ($\Delta T/T = |T_{\text{ref}} - T_i|/T_{\text{ref}}$) was derived, as illustrated in Fig. 14. An error of 57% on emissivity, resulting from the choice of a value 1 instead of 0.48, leads to a relative temperature uncertainty $\Delta T/T$ of 7.2%. Similarly, an error of 20% on emissivity only provides a relative temperature uncertainty $\Delta T/T$ of 2%.

Table 1 Temperature relative error $\Delta T/T$ at an observation distance of 3 m.

T_{ref} (°C)	350	375	400	425	450	475	500	525	550	575
T (°C)	355	377	403	429	453	476	501	526	553	577
$\frac{\Delta T}{T}$ (%)	1.4	0.5	0.75	0.95	0.66	0.21	0.2	0.19	0.543	0.345

2.3.4 *Influence of the blackbody orientation*

The influence of the location parameters of Eq. (2) was also analyzed. In the cargo area, a variation in the field of view angle θ_d between the blackbody and the camera, ranging from 0 to 40 deg, infers a low relative temperature error (0.15%).

Note that some experiments were carried out with interfering phenomena such as a powerful light (1000 W), a sampled light, and different fires. In each case, the overheat detection system is capable of detecting phenomena out of limit with a temperature higher than 600°C. The discrimination task between interfering phenomena and fires is carried out by the flame detection algorithm (see Sec. 4).

2.4 *Conclusion*

The overheat detection algorithm gives an alert by measuring the temperature increase of the flux produced by the phenomenon. The tests carried out demonstrated the ability to detect the beginning of an overheat situation from a temperature around 330°C with a relative temperature error below than ±12.5%C. Additional tests were conducted with blackbody temperature ranging from 350 to 575°C and at observation distance ranging from 3 to 10 m. The relative temperature error remains below than 6.5%. In a future version, the model of the temperature increase over a period of time could predict the phenomenon evolution and select the best configuration of the sensor, i.e., the right exposure time to measure a higher temperature.

3 Smoke Detection Algorithm

This section describes the camera mode of smoke detection and transmissivity measurements with the associated algorithm based on video image processing. The smoke detection mode is always active, in parallel with the overheat and flame detection algorithm, to prevent a hidden fire and to provide an additional parameter to discriminate fire from nuisance sources (interfering phenomena). In fact, smoke is the fire signature that is present as much in a smoldering as in a flaming combustion.

The term "smoke" defines the aerosols produced by the combustion reaction. Smoke aerosols vary widely in appearance and structure, from light colored during smoldering combustion, to black during flaming combustion. Aerosol size can vary from 0.01 to more than 10 μm and density from 10^2 to 10^6 particles/cm^3. These values depend on the combustion rate and the type of fuel.[16]

Photodetectors such as a video cameras operate on the extinction principle (reflection, diffusion, or absorption) of aerosol. This kind of detector is generally associated with a light source (typically a light-emitting diode in the visible or IR spectral band), which produces a beam that aerosols reflect, scatter, or absorb. The resulting signal in the photodetector, located near or in front of the light source, is proportional to the smoke particle properties (size and number of the particles in the sensing volume). Generally, the efficiency of the photodetectors depends on the diameter of the smoke particles D_p and the sensor wavelength λ in the ratio $(\pi D_p)/\lambda$. For example, if the ratio is larger than one, the forward diffusion on the smoke particles is the dominant effect. Next, the backward diffusion increases when the diameter of particles is smaller than the wavelength. Consequently, a forward diffusion detector is then particularly suited for detecting smoldering fire that is accompanied by relatively large smoke particles. These particles scatter forward much more light than the small particles produced in flaming combustions.

Table 2 Literature emissivity values.[14,15]

	Black Paint	Wood-Paper	Aluminum Paint	White Paint
ϵ	0.97–0.89	0.9–0.8	0.7–0.5	0.4

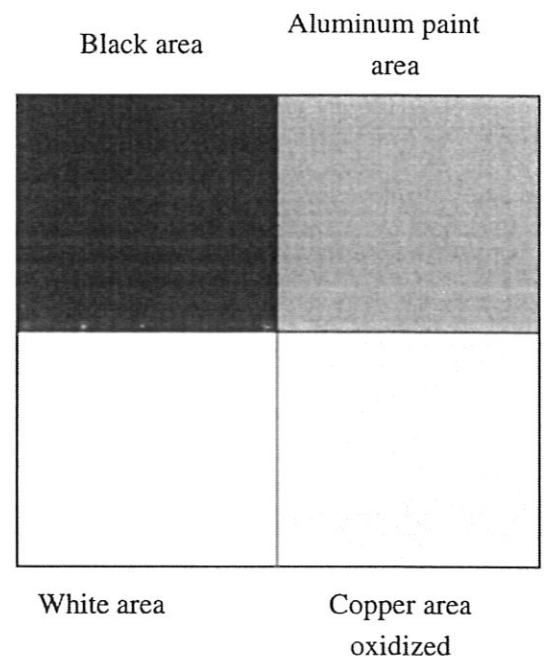

Fig. 13 Copper sheet with different emissivities.

Table 3 Experimental emissivity values.

	Black Area	Aluminum Area	Copper Area	White Area
ϵ	0.94±0.19	0.67±0.15	0.54±0.11	0.48±0.12

Moreover, photoelectric detectors monitor the light extinction coefficient with many signal analysis techniques. Three main techniques are (1) the histogram-based techniques[17] compare the computed histogram of the standard image with precomputed histograms of typical smoke scenes to determine the likelihood of smoke existence; (2) the temporal-based techniques[6] compute the difference and the segmentation between frames to detect and to identify a pattern that is the result of a smoke agglomerate (the patterns can be classified as smoke events); and (3) the rule-based techniques[8] also classify the smoke situation from a sequence of images to infer smoke presence.

The principle of our system consists in measuring the beam absorption from light reflected by specific targets which are illuminated with the active infrared source mounted on the VSU (see Fig. 15). The targets are horizontal and vertical reflectors placed in the top and the side of the cargo area (see Fig. 16). Finally, the system measures the attenuation of light over twice the distance between the light source, mounted on the camera, and the target. The ratio of attenuation rate is given by the ratio of the intensity I_D in presence of smoke and $I_{D\text{ref}}$ without smoke of the two regions of interest represented by the targets in the image as follows:

$$\frac{I_D}{I_{D\text{ref}}} = \exp[-(\sigma_e 2 d_s)]. \tag{4}$$

The ratio depends on the light extinction coefficient σ_e and the path length d_s (m) between camera and target.

This section outlines a first approach of the smoke algorithm. The detection principle is explained with the sensor configuration. The experiments and results are then described to determine smoke detection capability of the camera sensor.

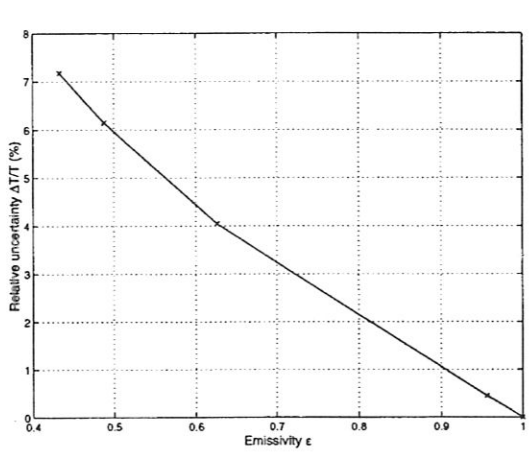

Fig. 14 Evolution of $\Delta T/T$ versus ϵ with a sheet temperature of 425°C and a sensor exposure time of 360 ms.

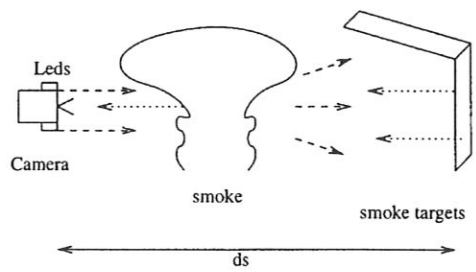

Fig. 15 Measurement principle of smoke.

3.1 *Detection Principle*

In a calibration procedure performed beforehand, an observation of noise system is performed to determine the signal standard deviation σ_{I_D}. These noise fluctuations establish the minimal intensity ratio $(I_{D\text{ref}} - 3\sigma_{I_D})/I_{D\text{ref}}$. For our system with a digitizer of 8 bits, a standard deviation σ_{I_D} of 1 gray level is estimated.

The initial step of the algorithm consists in measuring the reference image intensity $I_{D\text{ref}}$ without smoke between camera and smoke targets located vertically and horizontally in the cargo area. First, the algorithm extracts from the initial image the smoke targets, which are labeled as smoke region of interest (SROI). The system then measures the reference intensity $I_{D\text{ref}}$ of each region, which corresponds to the reflected luminance of the illuminated smoke targets. For smoke targets at a distance of 15 m, a maximal reference region intensity $I_{D\text{ref}}$ of 200 gray levels is measured with an exposure time of 8 ms. From the measurement of the signal standard deviation σ_{I_D}, a minimal intensity ratio $(I_{D\text{ref}} - 3\sigma_{I_D}/I_{D\text{ref}})$ of 0.985 can be deduced. Note that this ratio value corresponds to a light extinction coefficient from 0.015 to 0.001 m^{-1} for an observation distance from 1 to 15 m using Eq. (4). However, the light extinction coefficient vary from 0.6 to 1.5 m^{-1} in smoldering fire conditions[18] and from 0.04 to 0.3 m^{-1} in flaming

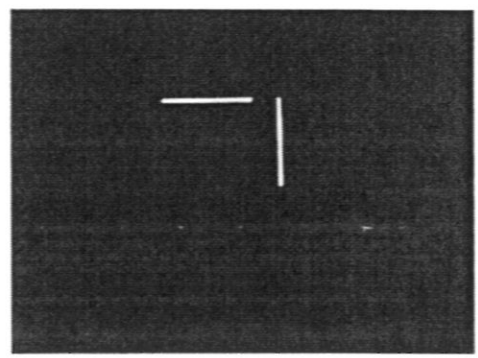

Fig. 16 Image of smoke targets in the NIR spectral band.

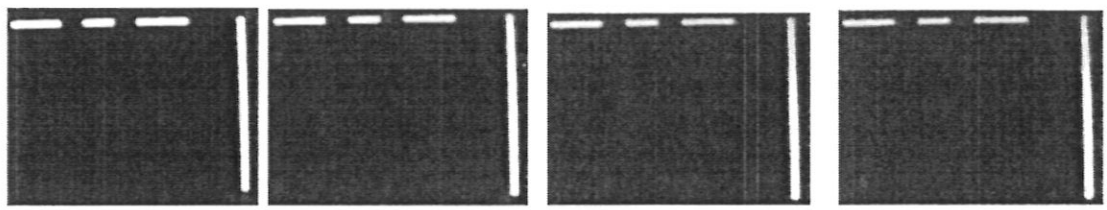

Reference image | Image at time of $t = 0\,ms$ | Image after a time of $t = 200\,ms$ | Image after a time of $t = 400\,ms$

Fig. 17 Smoke images at different times.

conditions.[19–21] In these conditions, the absorption effect produced from a smoldering or a flaming combustion can be detected. Moreover, a fit of the detection threshold ($3\sigma_{I_D}$ or $6\sigma_{I_D}$) enhances the false alarm immunity (e.g., alarms caused by dust or fog).

Next, the intensity I_D of each SROI is measured and the ratio $I_D/I_{D\text{ref}}$ is computed at video rate of 50 Hz. These ratio values are compared to the calibration data from smoke and nonsmoke situations. The detection time corresponds to various calibration situations that depend on the smoke targets distance from the camera. For each combination of location camera and smoke target, a minimal ratio is calibrated. Next, by observing the decrease of the intensity I_D that is produced from the absorption of smoke particles, it is possible in real time to measure smoke concentration versus time and to track obscuration rates (see Fig. 17). The measurement of the obscuration rate on the vertical target could be a discriminant parameter to distinguish smoke from fog.

Results from the smoke detection algorithm are given in the following subsection.

3.2 *Performance Evaluation*

Small-scale tests were performed with a specific smoke test chamber shown in Fig. 18 and large-scale tests with the cargo test cell shown in Fig. 11.

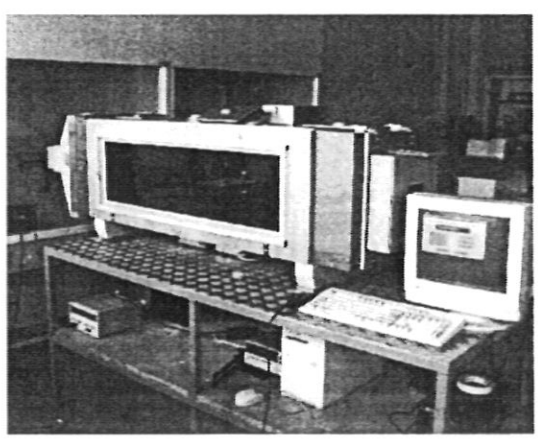

Fig. 18 Smoke chamber.

Open test-fires in smoldering and flaming conditions were performed with different hydrocarbons (kerosene, gasoline, etc.) and wood fires, according to the standard.[22,23] The produced smoke was not turbulently mixed with air.

In these conditions, the smoke detection algorithm was tested for smoke generated in and out of the camera's field of view (see Fig. 15). The detection times of the algorithm are summarized in Table 4 in some critical situations.

In the worst situations, the algorithm triggered an alarm 60 s after the beginning of the phenomenon. These laboratory measurements prove that the algorithm emits an alarm in the early stages of a real full-scale fire. Note that as visibility decreases rapidly after the alarm with a kerosene fire, it is difficult to monitor the cargo area. Moreover, the smoke of a cigarette located at a distance of 5 m from the detector is detected in a time below 1 min.

3.3 *Conclusion*

The tests carried out in this section have proven the feasibility of using a video camera for the detection and measurement of smoke concentrations. The smoke detection is accomplished via a video camera that analyzes the luminance from reflectors illuminated with an active IR source mounted on the camera. The reflectors placed in the cargo enable an early alarm in real fire conditions (hidden fire or fire in flaming conditions).

Further investigation is currently in progress to test the immunity of the smoke detection to fog conditions. The algorithm must distinguish between smoke and fog to avoid false alarms. In fact, fog produces water particles with similar characteristics as smoke in the NIR spectral band. The light extinction coefficient varies[24] from 6×10^{-4} to 0.15 m^{-1} with a diameter of water particles from 1 to 10 μm.[24] Observations must reveal a valuable discriminatory parameter for distinguish between attenuation due to smoke and that due to fog. The measurement of the obscuration rate versus time on the vertical target and the comparison between two systems should be developed and tested to distinguish smoke from fog.

After smoke detection, the flame detection algorithm, described in the next section, can be applied to investigate a fire situation.

Table 4 Smoke detection times in some critical conditions.

Distance (m)	Smoke from Generator in Field of View (s)	Smoke from Generator Out of Field of View	Smoke from Kerosene Fire in Flaming Conditions (s)
2	4	not performed	30
5	6	60 s	15
10	10	not performed	20

4 Flame Detection Algorithm

After an overheat and/or smoke detection, the flame detection algorithm must verify if a flame event is occurring. The event characterizes the transition of the smoldering and the flaming combustion.

In an open space, flaming fires emit radiation over a broad band of wavelengths (UV, visible, and IR emissions). The emissions correspond to an equivalent blackbody temperature[25] from 600 to 1200°C. Unlike hot spots, flame emissions are characterized by spatial fluctuations (see Fig. 19). In fact, the flame can be divided into two parts: the base of the flame, which is stationary, and the top which fluctuates with a specific puffing frequency (value in our application is around 4 Hz for a flame diameter[26] around 0.12 m). Moreover, the height of the flame then ranges from 0.2 to 0.5 m for the same flame diameter.[27] Finally, the flame detectable parameters, are temperature and the spatial fluctuations of the height of the flame.

In aircraft applications, flame radiation detectors use UV, visible, and IR flame emissions separately and in various combinations to discriminate nuisance sources like solar radiation.[28] In general, these radiation detectors are individual spot-type sensors and the cargo area is covered by a matrix coverage of these sensors. Another approach consists in surveying this large area with only one video sensor. A multispectrum video has been described in Ref. 29 that records images in the UV visible, and NIR spectral bands simultaneously. A video-based machine-vision fire detector has also been proposed and tested in a military aircraft cargo compartment.[9] The detector is a multispectrum video system that analyzes red, blue, green, and IR components of the image with color, IR, and microbolometer cameras. Image processing software is suggested to detect a variety of fires in the camera's field of view.

Our approach is to measure a specific set of flame parameters such as radiation, surface and frequency with a video system operating only in the NIR spectral band. Through the study of the frequency and the radiative intensity over a sequence of images, the proposed algorithm can detect and discriminate fire events from nuisance sources.

Based on the physical characteristics of a flame, this section describes the detection principle and measurement of characteristic properties of flame. The performance evaluation from standard test fires and nuisance sources are then conducted on a specific test cell.

4.1 *Detection Principle*

The algorithm principle is to analyze radiometric, spatial, and temporal characteristics of flame in a video sequence of N_T images acquired in the NIR spectral band with an exposure time of 0.1 ms. This time value captures images, as illustrated in Fig. 20, of the radiations from a low emission fire (alcohol fire) to a high one (kerosene fire). The radiation intensities are sampled at a video rate (frequency of 25 Hz), which is sufficient to measure the fire frequency around 4 Hz. The value of the sensor's spatial resolution is 65 mm at an observation distance of 10 m. This value represents a ratio between 1/3 and 1/8 of the flame height (depending on the fire sources). This sensor configuration detects flame events of all fire scenarios subjected to aeronautic standards.

After the detection of the flame event, multiparameters (temperature, spatial time variations, etc.) are measured over the image sequence. Finally, basic classification algorithms are used to determine if measured characteristics correspond to flame properties. This classification enables the rejection of common interfering signals such as reflected sunlight, lamps, etc.

4.1.1 *Flame detection*

The flame events are detected in the first image when the mean value of the image pixel I_D is greater than a threshold with corresponds to the minimal temperature of 600°C. After detection, the image pixels corresponding to this minimal temperature are labeled flame region of interest (FROI) of flame events. The first step is concluded by computing the minimal and maximal pixel digital intensity, number, size, hight, and center of gravity of each event from each image of the sequence. The image processing software has to extract higher level criteria from these initial informations to decide if a flame is present.

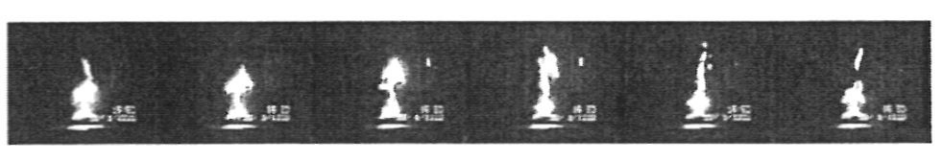

Fig. 19 Spatial fluctuations of acetone flame.

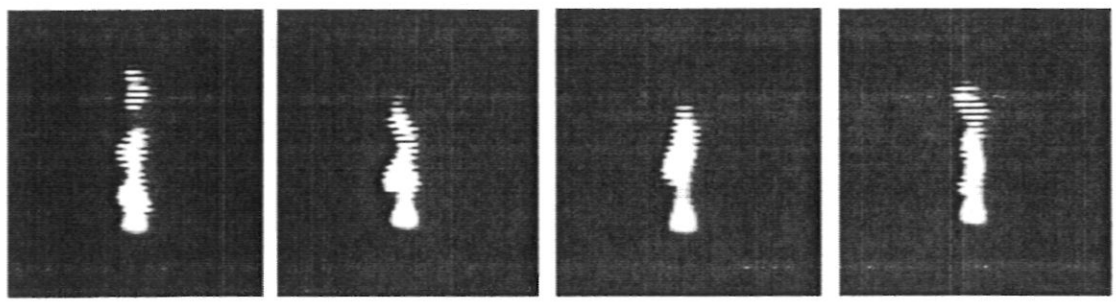

Image at time $t = 0\,ms$ Image after a time of $t = 40\,ms$ Image after a time of $t = 80\,ms$ Image after a time of $t = 120\,ms$

Fig. 20 Beginning of the flame image sequence.

4.1.2 *Temperature measurement*

After exhibiting the FROI in the first image, the first criterion computed is the flame temperature using an approach similar to the method used for overheat detection. For each image and each FROI, the radiometric model maps the nonsaturated pixels intensity I_D to an equivalent blackbody temperature value T as given in Eq. (1). In flame detection, unlike in overheat detection, the exact temperature of the source is not of great importance. The existence of an event with a blackbody equivalent temperature higher than 660°C is sufficient to indicate the probable presence of a flame. In addition, the radiation emitted by the flame and by the illuminated neighboring objects cannot be distinguished. All those parasite reflections may introduce errors of several hundred degrees in the temperature measurement. The indication of the equivalent blackbody temperature of different fire scenarios ranges from 700 to 800°C (see Table 5). Note that temperatures are lower at the flame extremities than at its center.

Flame presence can only be concluded with the computation of the spatial time variation features of the flame.

4.1.3 *Periodicity measurement*

Three criteria are defined to compute the flame spatial time variations. The first criterion is the periodicity P_f of the flame height H_f (see Fig. 21), which is computed in a finite sequence of N_T images. The sequence is sampled at the video rate of 25 Hz. For the finite sequence of images, a discrete Fourier transform breaks up this signal H_f into a sum of sinusoids and computes the power spectrum with an energy amplitude S. Note that F_p is the frequency of the highest energy amplitude and k its multiple; F_p ranges from 0 to the maximal frequency $F_{\max}=N_T/2\times F_e$, where F_e is the increment frequency ($F_e=25/N_T$ Hz). Also N_s is then the number of sinusoids present in the signal over the range $[0,F_{\max}]$. Finally, the periodicity P_f is defined by following the relation:[30]

$$P_f=\frac{\Sigma_{k=1}^{N_s}S(kF_p)-\Sigma_{k=1}^{N_s}S(kF_p+F_p/2)}{\Sigma_{k=1}^{N_s}S(kF_p)+\Sigma_{k=1}^{N_s}S(kF_p+F_p/2)}. \tag{5}$$

The periodicity provides a criterion signal with a value between 0 and 1.

Tests were performed with the data from $N_T=64$ images ($F_{\max}=12.5$ Hz and $F_e=0.39$ Hz) of different fire sources and nonfire stimuli. In accordance with JTSO standard,[31] nonfire stimuli are sources such as a 1000-W lamp, which represents the sun. A lamp interrupted by a chopper with a frequency lower than 5 Hz (see Fig. 22) is assumed to be a periodic source such as sun through an aperture. The computed values of the periodicity P_f of alcohol and kerosene fires vary from 0.7 to 0.8. Tests of wood and paper fires produce a periodicity value from 0.4 to 0.6. Note that the computed values of the periodicity can vary over 50% from the ignition to the extinction point of fires. The indicated values are recorded for flames in stationary development. Moreover, a lamp interrupted by a chopper at a frequency of 3.3 Hz produces periodicity value of 0.55, which corresponds to fire. The discrimination between acetone, alcohol, or kerosene fires and interfering phenomena is difficult with only the periodicity criterion. Moreover, a lower number of images (because of the memory requirements in an airborne application) damages the criterion performance. This low discrimination success rate associated with the

Table 5 Mean temperature T, intermittency I_f, and movement of the center of gravity of the flame C_B values for different fire sources.

Fire Sources	Kerosene	Gasoline Type A	Acetone	Alcohol	Wood	Paper
T (°C)	870–900	880–900	875–885	740–760	745–850	760–825
I_f	0.40–0.49	0.48–0.5	0.42–0.45	0.41–0.43	0.45–0.55	0.40–0.45
C_B	0.87	0.96	0.96	0.93	0.85	0.96

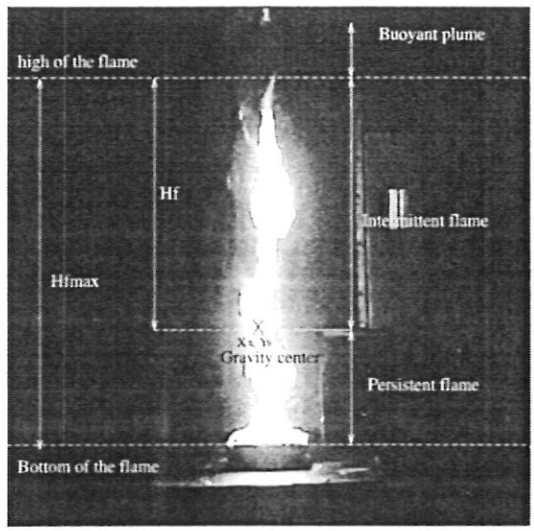

Fig. 21 Flame features: height, intermittency, threshold height, and center of gravity.

needs of a high number of images lead us to propose another criterion, the intermittency I_f (see Fig. 21).

As illustrated in Fig. 21, the intermittency[27] criterion I_f of flame height, which represents the flame presence probability. For a sequence of N_T images, the first process consists in performing the flame height H_f in each image ($i=1,...,N_T$) of the sequence and the mean value of the flame height $H_{f\text{mean}}$. In a second step, the ratio $\chi(i)=H_f(i)/H_{f\text{mean}}$ in each image ($i=1,...,N_T$) is provided. The third process consists in comparing each $\chi(i)$ to $\chi(j)$ of each image ($j=1,...,N_T$) and then, if $\chi(j)>\chi(i)$, the variable n_d is incremented. At the j end loop, the normalized intermittency $I_f(i)=n_d/N_T$ is computed. Note that a small value of $\chi(i)$ leads to $I_f(i)$ around 1, a high value of $\chi(i)$ leads to $I_f(i)$ around 0, respectively. The flame of the image i is then in the persistent region of flame, in the buoyant region, respectively.

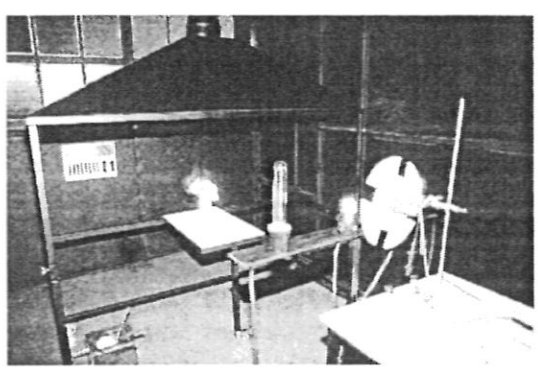

Fig. 22 Picture of the fire test.

The last process consists in performing the reference intermittency I_f for a value of $\chi(i)$ equal to 1. This value of intermittency then defines the probability of the flame height being superior to the mean height flame and characterizes a fire.

Every previous test combination of fire was repeated with intermittency criterion. The intermittency values range from 0.4 to 0.56 with a mean value $I_{f\text{mean}}$ of 0.47. For different fire scenarios, the uncertainty of $I_{f\text{mean}}$ is only of ± 0.057. In addition, the intermittency value ranges from 0 to 0.22 for nuisance sources such as sun, sampled sun, and different colored lights. In conclusion, the intermittency criterion contains useful information for discriminating between fire and nonfire stimuli.

Robust detection can be obtained by adding a third criterion, the movement of the gravity center of the flame (see Fig. 21). The first process consists in performing the center of gravity of the flame $[x_B(i),y_B(i)]$, in each image ($i=1,...,N_T$) of the sequence. At the end, the mean value (x_C,y_C) of all centers of gravity $[x_B(i),y_B(i)]$ is computed. The second process consists in computing the Euclidean distance $L_B(i)$ between the coordinates of the center of gravity $[x_B(i),y_B(i)]$ of each image and the mean value of all centers of gravity (x_C,y_C) as follows:

$$L_B(i)=\{[x_B(i)-x_C]^2+[y_B(i)-y_C]^2\}^{1/2} \quad \text{with} \quad i\in[1,...,N_T]. \tag{6}$$

In conditions of unvarying phenomenon, the spatial fluctuations of the centers of gravity $[x_B(i),y_B(i)]$ depend only on spatial detector noise. In a sequence of N_T images, the spatial noise detector is characterized by a circle that includes all the fluctuations of the center of gravity positions. This "noise" circle is defined by its radius R_B. Moreover, in conditions of fluctuating phenomenon, if $L_B(i)$ is higher than R_B, the variable of the center of gravity movement of the flame $n_B(i)$ in each image receives the value 1 else value 0. Finally, the criterion of the movement of the center of gravity of the flame C_B is computed as follows:

$$C_B=\frac{\Sigma_{i=1}^{N_T} n_B(i)}{N_T}. \tag{7}$$

Note that distances $L_B(i)$ are less than the height of the flame H_f. The detector spatial resolution can limit the computation of the criterion of the movement of the center of gravity. In addition, the criterion of the movement of the center of gravity of the flame is applied only if a FROI is detected (i.e., a flame event is detected in the image). For a lamp interrupted by a chopper, the criterion is computed if the flashing light is visible.

Finally, a standard classification algorithm based on temperature, intermittency, and movement of the center of gravity of the flame is used to determine if the detected event is consistent with a flame. The multicriteria fire analysis is now applied to all test fires used in EN 54 part 9 standards.

Table 6 Temperature T, intermittency I_f, and movement of the center of gravity of the flame C_B values for different nonfire sources.

Nonfire Sources	Yellow Light	Red Light	Light (Power 1000 W)	Sampled Light
T (°C)	868	828	Saturation	—
I_f	0	0	0	0.18–0.22
C_B	0–0.1	0–0.1	0	0.25

4.2 *Performance Evaluation*

The objective is to evaluate our new sensing technology associated to the image processing software to detect fires and nonfire stimuli in cargo compartment. The evaluation was performed according to the aeronautic standards.[23] This document applies to a minimum performance standard and validation for digital computer. The standards require to detect the flame in 1 min from the start of different fire scenarios. The specific test cell to emulate the different scenario is first presented. The performances of our system are then described.

In the cell test structure of an aircraft cargo compartment (see Fig. 11), a specific fire test was built to simulate the conditions of fire and nonfire sources (see Fig. 22). Fire sources were generated by a flaming of wood and paper in a specific burner and liquid fuels (kerosene, acetone, etc.) in a specific pan with a diameter D_f of 0.12 m. Nuisance sources were emulated by red, yellow and high power lights and by a sampled light with a power of 1000 W.

Large-scale experiments were conducted in the specific test cell. Each experiments of fire were repeated several times to develop a statistically meaningful data base for each type of fire. The flame properties (mean temperature T, intermittency I_f, and movement of the center of gravity of the flame C_B) were computed over a sequence of $N_T = 32$ images of fire and nonfire sources. These results computed for a fire-camera distance of 10 m are recorded in Tables 5 and 6.

Note that the difference of the mean equivalent blackbody temperature is small between different fire sources. In fact, the temperature is measured only for nonsaturated pixels. Moreover, these values are not real flame temperature because the emissivity of the flame is not considered. Criteria of spatial time variations are necessary in the classification algorithm for discriminating fire and non-fire sources (see Fig. 23). The figure shows that the sources can be separated into two categories. The discrimination between the two categories comes easily.

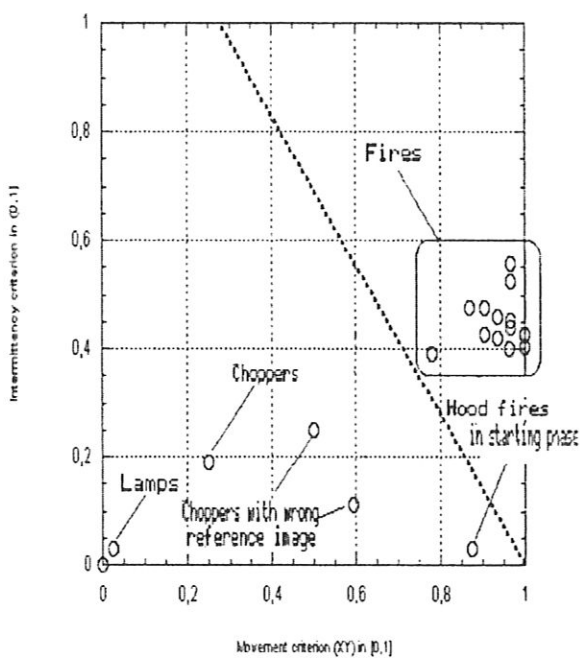

Fig. 23 Fire discrimination from intermittency criterion I_f and movement criterion C_B.

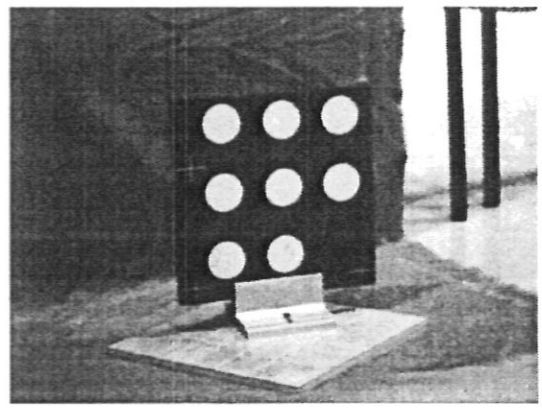

Fig. 24 Load target.

4.3 *Conclusion*

Based on the test results reported in previous section, it is concluded that it is feasible for the same detector, a CCD camera operating in the NIR, to measure small temperature gradient in overheat conditions and high temperature in flame detection. Next, it is also feasible to discriminate fire and nonfire sources with an analysis of the time variation of the flame radiations. Temperature, intermittency, and movement measurements enable us to distinguish flame characteristics from nuisance sources properties.

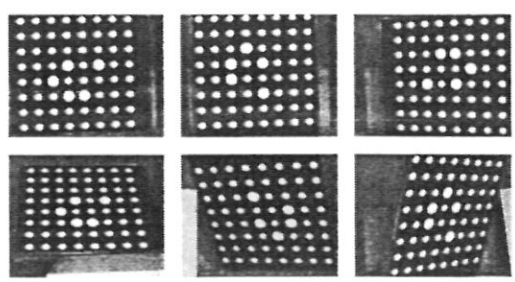

Fig. 25 Calibration using multiple views of a planar pattern.

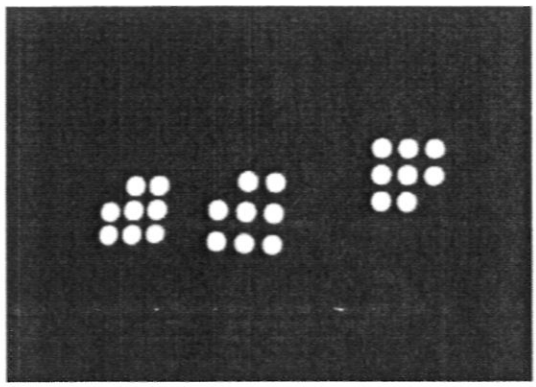

Fig. 26 Multiple target recognition.

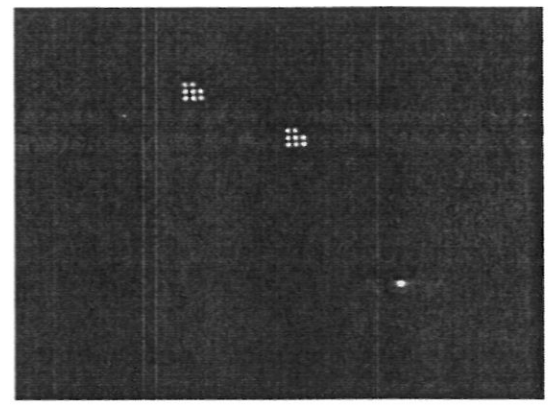

Fig. 28 Initial image (two patterns to be detected and an artifact).

5 Load Displacement Detection Algorithm

The load displacement system must detect a minimal movement of 50 mm at an observation distance of 15 m of the freight in the aircraft cargo holds. The system must also measure its amplitude (higher than 50 mm) with a relative uncertainty of 10%.

The load displacement detection must be accomplished with the video sensor operating in the NIR spectral band (the filter used in the overheat and the flame algorithms cannot be removed). The detection is then performed with the reflected luminance from the loads, which are illuminated with an active infrared source mounted on the camera. Moreover, for cost and maintenance reasons, the displacement measurement must be performed in the field of view of one camera. The load position with respect to the video sensor can be only computed with a monocular vision approach. With these conditions, it is necessary to know the 3-D geometric model of loads. For an application concerning the monitoring of free-form objects, two solutions can be tested to know the geometric model of load. It can be learnt in the loading step or a specific visual pattern can be fixed on each load. For robustness reasons, we have chosen to equip each load with a known specific target with a pattern composed of eight reflective patches with diameter of 50 mm. The pattern has been designed in order to allow an automatic estimation of the load orientation (see Fig. 24). The principle of the displacement measurement is to localize in 3-D the target pattern between two successive image acquisitions. First, we must detect the pattern illuminated with the active infrared source mounted on the camera. The load detection principle and the physical model of the VSU have been presented in Ref. 10. Next, the localization of the pattern can be computed only if the geometric model of the imaging sensor is also determined. The geometric model based on "pinhole" model presented in Ref. 32 and the associated calibration procedures for a CCD camera operating in the NIR spectral band are described in Ref. 10. For our application involving accurate dimensional measurements, a specific flexible technique has been used, as described in Ref. 33, which requires only the camera to observe a quasi-planar pattern presented with different orientations (see Fig. 25). The motion of the pattern need not be known and the pattern itself can be imprecise. The calibration procedure provides the intrinsic parameters of the camera that will be used by the 3-D localization method. Finally, if we suppose that the camera has already been calibrated beforehand, the target localization with respect to the camera is computed from the 3-D geometric model of the target, which has been previously learned. In the end, the displacement is computed between two successive target localization.

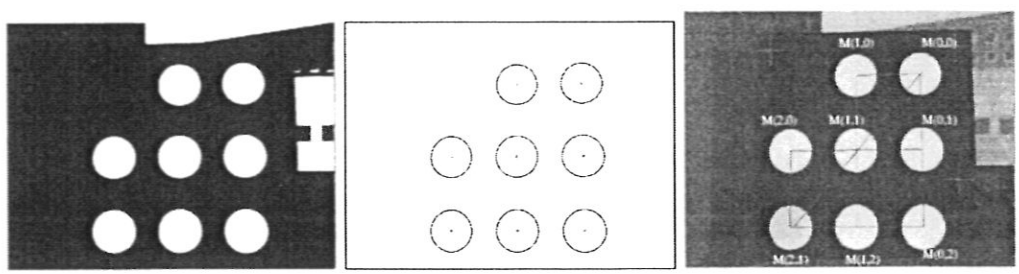

(a) (b) (c)

Fig. 27 Pattern recognition procedure: (a) binarized image, (b) contour extraction and ellipse fitting, and (c) successful recognition of the pattern.

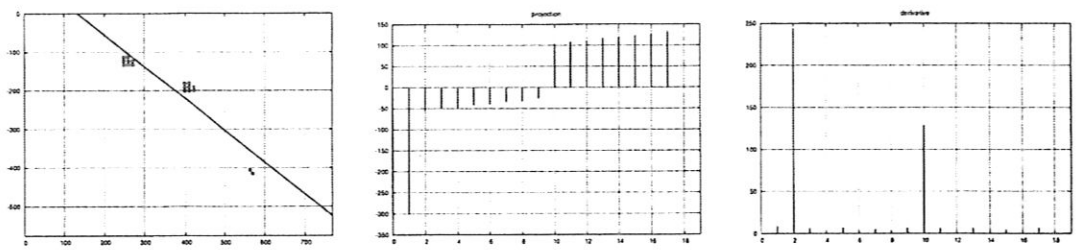

(a) (b) (c)

Fig. 29 First iteration of the multiple target recognition procedure: (a) step 1, first principal axis; (b) step 2, first principal component values; and (c) step 3, differences between adjacent first principal component values.

The section describes the detection and the recognition of all the targets that lie in the scene. Next, it presents the 3-D localization of the target pattern and the computation of the target displacement. Finally, a performance evaluation is conducted with the influence of the distance and the target orientation.

5.1 *Detection and Recognition of the Target Pattern*

Before the takeoff phase, a reference image of the cargo area is recorded. During the flight, in real time, each image of the targets (one target per load) illuminated by the active IR source is analyzed to detect and recognize them. Note that an exposure time of 20 ms is sufficient to extract the eight reflective patches of the pattern (see Fig. 26). This exposure time allows a video rate detection. The single and multi-target recognition algorithms are presented below.

5.1.1 *Single-target recognition*

First, the algorithm performs a binarization of the image with automatic threshold selection.[34] Then a region labeling is performed. After a contour extraction in the labeled image, a method based on ellipse fitting[35] and region filtering with a shape criterion gives the center and the principle axis of the patches with a subpixel accuracy. Finally, an operation of pattern matching concludes the target recognition phase which relies on straight interactions of lining up ellipses. Figure 27 summarizes the different operations.

5.1.2 *Multiple-target recognition*

The multipattern recognition algorithm is based on a principal component analysis (PCA) approach.

An analysis of the image is performed to separate all the contours of the image in clusters of eight contours (the pattern is made up of eight reflective patches). Each cluster is then tested to determine if it is a true pattern or an artifact.

A region segmentation of the image is first performed. The contour of each region is then computed and approximated by an ellipse.[35] Using the residual value of the approximation, a filtering operation is performed to discard the contours that cannot be an ellipse (residual value too high). Each kept contour (it is probably an ellipse and might correspond to a patch of a possible target) is then represented by a 4-D data vector containing: the center of gravity of the ellipse (i,j), the surface of the ellipse (S_e), and the distance to the nearest ellipse in the image (D_e). Note that the pattern is characterized by eight reflective patches of the same size (i.e., same surface) and same distance between patches: the surface of the contours and their inter-distance are relevant factors for the pattern recognition.

Finally, for all the contours, a recursive algorithm is then performed in the 4-D space:

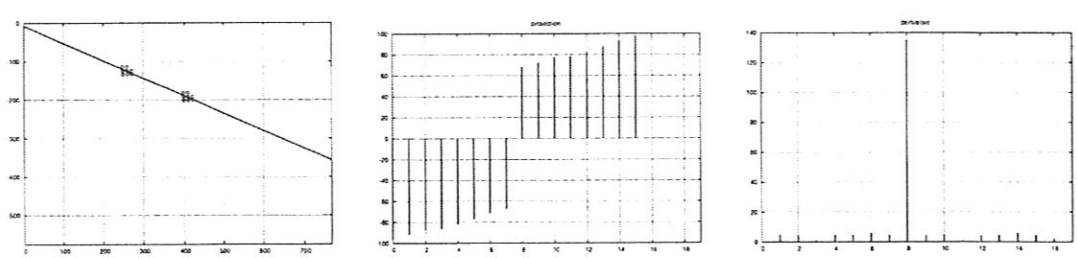

(a) (b) (c)

Fig. 30 Second iteration of the multiple target recognition procedure: (a) step 1, first principal axis; (b) step 2, first principal component values; and (c) step 3, differences between adjacent first principal component values.

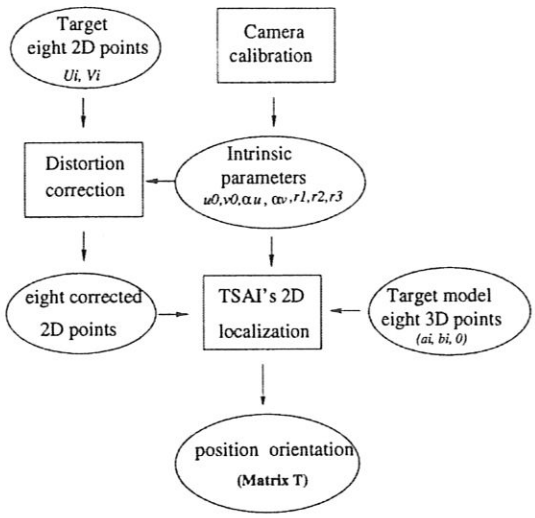

Fig. 31 Target 3-D localization method.

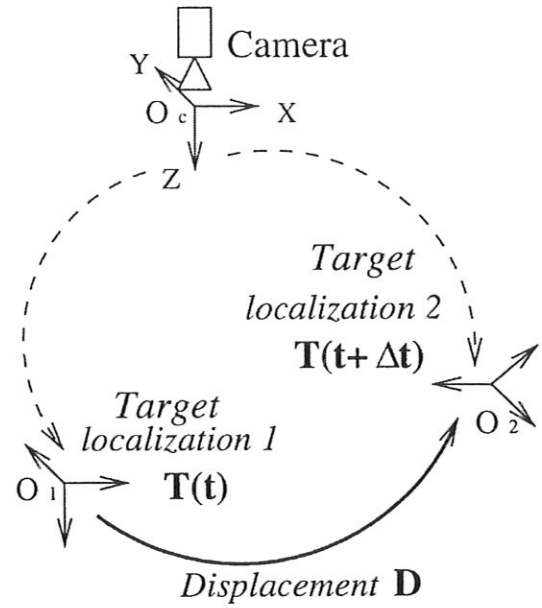

Fig. 32 Target displacement **D** from two successive localizations at time t and $t+\Delta t$.

1. The direction of the first principal component is first computed.
2. The 4-D data vectors are projected on the first principal axis, giving principal component values.
3. The differences between adjacent principal component values (derivative) are computed, and the location of the maximum difference is used to separate the contours into two groups.
4. Steps 1 to 3 are repeated for both groups.

Steps 1 to 4 are repeated until all the contours have been separated in clusters containing eight contours or less.

At the end of the algorithm, we get a number of cluster of eight contours or less. All the clusters with less than eight contours are discarded as they are not patterns. Using the single-target recognition algorithm (see Sec. 5.1.1), each cluster of eight contours (a possible pattern) is tested in order to determine if it is a true pattern or an artifact.

As an example, the algorithm is performed on the image of Fig. 28, which represents two patterns and an artifact.

It is not easy to visualise data in 4-D space so in order to explain how the algorithm works each contour is represented by a data vector (its center of gravity). Figure 29 illustrates the steps of the first iteration of the algorithm. Figure 29(a) gives 2-D data vectors and first principal axis (two patterns made up of eight contours and two contours corresponding to an artifact); Fig. 29(b) shows the first principal component values; Fig. 29(c) shows the differences between adjacent first principal component values of Fig. 29(b).

Figure 30 illustrates the steps of the second iteration of the algorithm: Fig. 30(a) gives 2-D data vectors and first principal component of the remaining points; Fig. 30(b) shows the first principal component values; Fig. 30(c) proposes the differences between adjacent first principal component values of Fig. 30(b). At the end of the algorithm two patterns have been identified and the artifact has been discarded.

5.2 *3-D Localization of the Target Pattern*

The 3-D localization of each pattern is performed using Tsai's localization method[36] applied to a 2-D object. The method requires the 3-D object geometric model, the eight extracted center of the patches $\{\mathbf{m}_i=(u_i,v_i)^T$, where $i \in [0,7]\}$ and the knowledge of camera intrinsic parameters. Tsai's technique is based on a distortion-free pinhole camera model. Therefore, we must correct the feature-extracted points of the pattern from their distortion before using it. This correction is performed using the intrinsic parameters provided by the calibration procedure applied in the NIR spectral band (see Fig. 31). Using the relation between the eight corrected points $[\mathbf{m}_{ri}=(u_{ri},v_{ri})^T]$ and the eight 3-D

Table 7 Relative error $\Delta d/d$ with vertical displacements.

d_{ref} (mm)	50	100	150	200	250	300	350	400	450	500
d (mm)	50.65	99.95	151.21	201.54	248.87	299.61	348.49	397.82	443.80	495.03
$\frac{\Delta d}{d}$ (%)	1.3	0.05	0.8	0.8	0.5	0.1	0.4	0.5	1.3	1.0

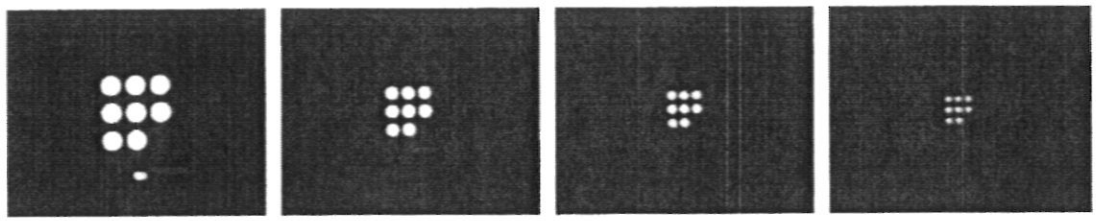

$d = 4m$ $d = 6m$ $d = 8m$ $d = 10m$

Fig. 33 Influence of the load camera distance.

target points $[\mathbf{M}_i=(a_i,b_i,0)^T]$, the technique computes the position $\mathbf{t}$ and the orientation $\mathbf{R}$ of the target and then, provides the localization matrix

$$\mathbf{T}=\begin{pmatrix}\mathbf{R} & \mathbf{t}\\ 0 & 1\end{pmatrix}.$$

Finally, the target displacement $\mathbf{D}$ (see Fig. 32) is performed from two successive localizations (localization 1 and localization 2) following the relation:

$$\mathbf{D}=\mathbf{T}^{-1}(t)\mathbf{T}(t+\Delta t)=\begin{pmatrix}\mathbf{R}_{12} & \mathbf{t}_{12}\\ 0 & 1\end{pmatrix}, \tag{8}$$

where $\mathbf{R}_{12}$ is the rotation matrix between localization 1 and 2 and $\mathbf{t}_{12}$ is the displacement vector between localization 1 and 2. From $\mathbf{D}$, we can compute the rotation of the load $(\mathbf{R}_{12})$ and its displacement norm $d=\|\mathbf{t}_{12}\|=\|\mathbf{O}_1\mathbf{O}_2\|$.

5.3 *Performance Evaluation*

To evaluate the performance of the system with respect to the displacement measurement accuracy, we have moved the target in the view field of the camera using an accurate XYZ translation setup.

For each displacement, the relative error is computed using the following relation:

$$\frac{\Delta d}{d}=\frac{|d_{\text{ref}}-d|}{d_{\text{ref}}}, \tag{9}$$

where $d=\|\mathbf{t}_{12}\|=\|\mathbf{O}_1\mathbf{O}_2\|$ is the measured displacement norm, and d_{ref} the reference displacement. Using this criterion, we have also analyzed the influence of the load camera distance and the target orientation.

5.3.1 *Displacements orthogonal to the optical axis*

The target was placed at a distance d_s of 3 m from the camera. The target is then translated vertically and horizontally in the view field of the camera from the threshold detection of 50 to 500 mm with increments of 50 mm.

Table 7 proves that the obtained relative error $\Delta d/d$ with vertical displacements is less than 1.3%. Same experiments have been carried out with horizontal displacements and the relative error is less than 0.8%.

5.3.2 *Influence of the load camera distance*

The previous tests were repeated with the target placed at different distances of the camera, respectively, 4, 6, 8, and 10 m (see Fig. 33).

For the target placed at distance below than 6 m far from the camera, the relative error $\Delta d/d$ has been found to be less than 5%. For higher target-camera distances, the relative error $\Delta d/d$ has raised and has climbed to 30%. Note that the camera was focused at a distance of 6 m. In the future, it could be interesting to mount an autofocus lens, or to control the focus by the computer, so that the estimation could not become worse for larger depths. The problem would be then more complicated because the camera intrinsics parameters would vary.

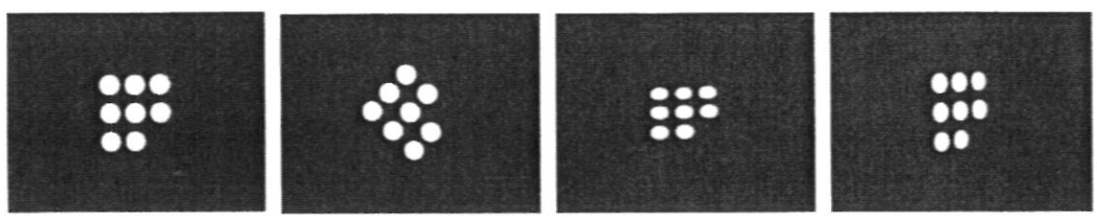

Initial position Z-rotation Y-rotation X-rotation

Fig. 34 Influence of the target orientation.

Table 8 Measurement of target orientation.

Imposed Orientation (*X*, *Y*, and *Z* Rotations) (deg)	Measured Orientation (deg)		
	X Rotation	*Y* Rotation	*Z* Rotation
15	16	13	17
30	32	30	33
45	47	46	48
60	61	58	63

5.3.3 *Influence of the target orientation*

It is unlikely that the target can be fixed to the load in a position parallel to the camera image plane. Thus, the aim of this test was to verify that the system is able to detect and measure vertical and horizontal displacements of the target even if the target is not parallel to the camera image plane. Tests of displacements orthogonal to the optical axis have been then performed with different orientations of the target (see Fig. 34). This target was placed $3m$ far from the camera. It was rotated, tilted and panned (0 to 60 deg) and then, moved vertically and horizontally in the view field of the camera. The measured relative error $\Delta d/d$ has proved to be less than 1.9%.

5.3.4 *Measurement of target orientation*

The localization matrix provides the orientation and the position of the target. The displacement matrix [see Eq. (8)] provides the rotation **R** of the load between two successive localizations. We have performed several tests to verify that the system is able to detect and measure a rotation of the load (see Fig. 34). From Table 8, we can see that the relative accuracy is better than 10%.

5.3.5 *Multiple targets detection in presence of artifacts*

Finally, we performed some tests with multiple targets and we added some artifacts in the view field of the camera to evaluate the robustness of the algorithm (see Fig. 35). The patterns were successfully recognized and the artifacts rejected.

5.4 *Remark*

Note that using a single camera is not the best way to tackle 3-D localization problems. A stereo-vision approach[37] would give better results especially with regards to displacements along the optical axis of the camera. For cost saving reasons, we have decided to develop a single-camera-based system.

6 Conclusion

The main achievement of the work presented in this paper is demonstrating that a single sensor, a CCD camera operating in the NIR spectral band, associated with specific algorithms can simultaneously visualize, detect, and measure the properties of the whole range of fire signatures (overheating, smoke and flame) as well as freight movements in aircraft applications.

The first candidate fire signature, presence of overheating, is detected and characterized by a NIR radiation measurement. The detection tests proved that the CCD camera associated with the proposed overheat detection algorithm were able to detect overheating conditions generated with a blackbody from a temperature of 300°C. The blackbody equivalent temperatures ranging from 350 to 575°C were measured with a maximal relative error of 6.5%. Additionally, the minimal size of hot spots detected is 65 mm at an observation distance of 10 m. The result is a thermal image where the measured image intensity values of hot spots are mapped to blackbody equivalent temperature values.

As for the second fire signature, presence of smoke, detection is based on a transmissivity measurement between the CCD camera and specific reflectors illuminated with a NIR source mounted on the camera. Tests performed in a custom-built smoke-test facility proved that in a worst case scenario of concealed fire, the detection time is less than 1

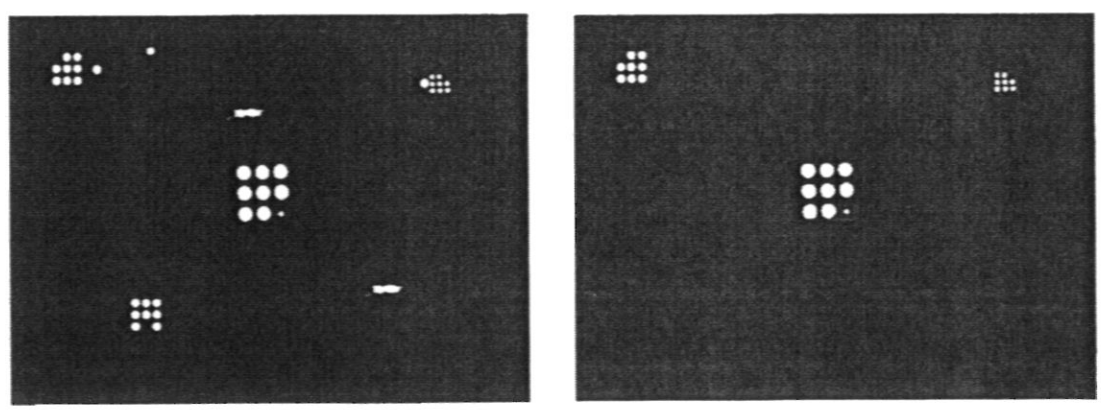

(a) (b)

Fig. 35 Multiple targets detection: (a) binarized image and (b) successful recognition of three targets (three loads).

min. This time value is obtained when the obscuration measurement falls below a threshold corresponding to sensor noise.

Detection of the presence of flame, third on our list of fire signatures, is achieved by a combination of radiation and time-variation measurements of the flame itself. The detection algorithm is based on temperature measurement and two criteria of flame periodicity. Tests, conducted according to aeronautical standards, proved that these multiparameter computations in a sequence of 32 images were able to detect all types of flame and differentiate them from nuisance radiation sources, such as sunlight.

Another significant result is the performance of the proposed surveillance system in the detection of freight movements in the cargo hold. The proposed load displacement algorithm is based on a 3-D localizations of load in two images. This technique enables the measure of vertically and horizontally load displacements from 50 to 500 mm with a maximal uncertainty of 5% at an observation distance below than 6 m. For higher observation distances, the camera is not under focus and the uncertainty increases to 30%.

The paper has presented a system, comprised of a sensor and associated software, with multiparameter detection and measurement capabilities, enabling the protection of an aircraft cargo compartment against fire and freight movement. The performance evaluation of the system proves the ability to measure a large range of fire parameters simultaneously and with a high degree of sensitivity. The high resolution of the sensor also enables the measurement of small spatial fluctuations in the phenomenon. The trials, having been performed according to the stringent standards of the aeronautics industry, show the system to be an ideal choice for large-body aircraft cargo bays such as on the Airbus 380. Current systems employing a number of individual spot-type sensors can be replaced with this single sensor, enabling considerable cost savings, along with the improvements in performance and maintenance facility. With such a level of technical performance it is evident that the system will excite interest in other fields where surveillance requires multiparameter detection.

To extend this project, two refinements could further improve the accuracy of the measurements. First, the discrimination between smoke and fog should be developed by adding a temporal obscuration rate. Second, a temperature prediction step would improve the phenomenon tracking by allowing a better control of the sensor potentialities.

Acknowledgments

The authors wish to thank J. P. Arcens and B. David from École des Mines d'Albi-Carmaux, and C. Goin and G. Baudelet from Latécoère group for their technical help. We also thank D. Garcia and P. Gaborit from École des Mines d'Albi-Carmaux for their help in the development of the single and multiple patterns recognition algorithms. The authors wish to thank the reviewers for their careful reading and their helpful comments. This research was supported by Latécoère group.

References

1. A. Grandison, R. Mawhinney, E. Galea, M. K. Patel, E. Keramida, A. Boudouvis, and N. Markatos, "The FIREDASS (fire detection and suppression simulation) model," in *Proc. Int. Aircraft Fire and Cabin Safety Research Conf.*, Federal Aviation Administration, Atlantic City, NJ (Nov. 1998).
2. T. Grabow, "New fire smoke detection and fire extinguishing systems for aircraft applications," in *Proc. Int. Aircraft Systems Fire Protection Working Group (IASFPWG)*, Federal Aviation Administration, (Mar. 2001).
3. D. Blake, J. O'Sullivan, S. Hammann, M. Kolleck, and T. G. Cleary, "Aircraft cargo area fire detection," in *NIST Fire Detector Workshop Proc.*, pp. 9–13, National Technical Information Service (NTIS). U.S. Department of Commerce, Springfield, VA (Dec. 1997).
4. A. D. Goedeke, B. Drda, S. Viglione, and G. Gross, "Fire detection system—us patent 005153722a," Tech. Rep., Donmar Ltd., Newport Beach (Jan. 1991).
5. J. A. Neal, C. E. Land, R. R. Avent, and R. J. Churchill, "Application of artificial neural networks to machine vision flame detection," Tech. Rep., American Research Corporation of Virginia, Radford (Apr. 1991).
6. A. Donald Goedeke, C. Fitzpatrick, and Glenn E. Healey, "Cost effective, dual purpose machine vision-based detectors for: (1) smoke and flame detection, and (2) engine overheat/burn through and flame detection," Tech. Rep., Donmar Ltd., Newport Beach (Mar. 1995).
7. O. A. Plumb and R. F. Richards, "Development of an economical video based fire detection and location system," Tech. Rep. NIST GCR 96-695, National Technical Information Service (NTIS), Gaithersburg, MD (July 1996).
8. S. Y. Foo, "Fuzzy logic approach to fire detection in aircraft dry bays and engine compartments," *IEEE Trans. Ind. Electron. Control Instrum.* **47**(5), 1161–1171 (2000).
9. A. D. Goedeke, "Cost effective multi-purpose machine vision based fire smoke and engine overheat detectors," Tech. Rep., Air Force Contract No. F33615-95-C-3407 (Feb. 1998).
10. T. Sentenac, Y. Le Maoult, J. J. Orteu, and G. Boucourt, "Evaluation of a CCD based video sensor for aircraft cargo surveillance," *Opt. Eng.* **41**(4), 796–809 (2002).
11. G. Boucourt, "Device for monitoring an enclosure, in particular the hold of an aircraft—patent PCT/FR99/00446," Tech. Rep., Latécoère, Toulouse, France (Jan. 1999).
12. T. J. Ohlemiller, *Smoldering Combustion*, Vol. Section 2, Chap. 11, of *SFPE Handbook of Fire Protection Engineering*, 2nd ed. (1995).
13. L. Wang, C. Zhu, and J. Whang, "A new type of intelligent point photoelectric smoke-heat combined fire detector," in *Proc. Int. Conf. on Automatic Fire Detection, AUBE 1999*, Gerhard-Mercator, Ed., pp. 262–271, University of Duisburg, Germany (Mar. 1999).
14. M. J. Modest, Ed., *Radiative Heat Transfer*, McGraw-Hill, New York (1993).
15. F. Incropera and D. De Witt, *Fundamentals of Heat and Mass Transfer*, Wiley, New York (1985).
16. G. W. Mulholland, *Smoke Production and Properties*, Vol. Section 2, Chap. 15, *SFPE Handbook of Fire Protection Engineering*, 2nd ed., National Fire Protection Association (1995).
17. G. E. Healey and R. Kondepudy, "Radiometric CCD camera calibration and noise estimation," *IEEE Trans. Pattern Anal. Mach. Intell.* **16**(3), 267–276 (1994).
18. J. D. Seader and I. N. Einhorn, "Titre," in *Proc. 16th Int. Symp. on Combustion*, p. 1423, Combustion Institute, Pittsburgh, PA (1977).
19. R. A. Dobbins, G. W. Mulholland, and N. P. Bryner, "Comparison of a fractal smoke optics model with light extinction measurements," *Atmos. Environ.* **28**(5), 889–897 (1994).
20. G. W. Mulholland and M. Y. Choi, "Measurement of the mass specific extinction coefficient for acetylene and ethene smoke using the large agglomerate optics facility," in *Proc. 27th Int. Symp. on Combustion*, Vol. 1, pp. 1515–1522, Combustion Institute, Pittsburgh, PA (Aug. 1998).
21. G. W. Mulholland and C. Croarkin, "Specific extinction coefficient of flame generated smoke," *Fire Mater.* **24**(5), 227–230 (2000).
22. Afnor, "S61-954-EN54-7. European requirements for industrial fire warning systems," Tech. Rep., Association française de normalisation (Afnor), Paris (1989).
23. Afnor, "S61-956-EN54-9. European requirements for industrial fire warning systems," Tech. Rep., Association française de normalisation (Afnor), Tour Europe Cedex 7 92 049 Paris La Défense, France (Mar. 1997).
24. G. Gaussorgues, *La Thermographie Infrarouge*, Lavoisier, (1989).
25. D. Drysdale, Ed., *An Introduction to Fire Dynamics*, Wiley, New York (1994).
26. G. Cox and R. Chutty, "A study of the deterministic properties of unbounded fire plumes," *Combust. Flame J.* **39**, 191–209 (1980).
27. E. E. Zukoski, B. M. Cetegen, and T. Kubota, "Visible structure of buoyant diffusion flames," in *Proc. 20th Symp. on Combustion*, pp. 361–366, The Combustion Institute (1984).
28. Cerberus, "The leading edge in airborne smoke detection," Tech. Rep., Cerberus Guinard, France (Jan. 1998).
29. D. Kozeki, "Smoldering fire detection by image processing," in *Proc. Conf. on Automatic Fire Detection, AUBE 2001*, pp. 71–78, National Institute of Standards and Technology, Eds., Gaithersburg, MD (Oct. 2001).

30. P. Ramprasad and C. N. Randal, "Detection and recognition of periodic nonrigid motion," *Int. J. Comput. Vis.* **23**, 261–282 (1997).
31. Federal Aviation Agency Standard, "Joint aviation requirements, joint technical standard order," Tech. Rep., Federal Aviation Administration Standards (FAA), U.S. Government Printing Office, Washington, DC (June 1991).
32. O. D. Faugeras, *Three-Dimensional Computer Vision: A Geometric View Point*, The MIT Press (1993).
33. D. Garcia, J. J. Orteu, and M. Devy, "Accurate calibration of a stereovision sensor: comparison of different approaches," in *Vision, Modeling, and Visualization 2000*, Saarbrücken, Germany (Nov. 2000).
34. N. Otsu, "A threshold selection method from gray-level histograms," *IEEE Trans. Syst. Man Cybern.* **1**, 62–66 (1979).
35. Z. Zhang, "Parameter estimation techniques: a tutorial with application to conic fitting," Tech. Rep. 2676, INRIA (Oct. 1995).
36. R. Y. Tsai, "A versatile camera calibration technique for hight-accuracy 3D machine vision metrology using off-the-shelf TV cameras and lenses," *IEEE J. Rob. Autom.* **RA-3**(4), 323–344 (1987).
37. D. Garcia, J. J. Orteu, and L. Penazzi, "A combined temporal tracking and stereocorrelation technique for accurate measurement of 3D displacements: application to sheet metal forming," *J. Mater. Process. Technol.* **125–126**, 736–742 (2002).